Published in Water Resources Research 53, 8512-8532, 2017
which should be used for any reference to this work

Simulating Small-Scale Rainfall Fields Conditioned by Weather State and Elevation: A Data-Driven Approach Based on Rainfall Radar Images

Key Points:
- We propose a novel methodology to simulate 1 km resolution daily rainfall fields
- The simulations are conditioned by daily weather indicators and topographic elevation
- The method can simulate realistic rainfall patterns in space and explore the temporal variability

Correspondence to:
F. Oriani,
fabio.oriani@protonmail.com

Fabio Oriani[1,2], Noa Ohana-Levi[3], Francesco Marra[4], Julien Straubhaar[1], Gregoire Mariethoz[5], Philippe Renard[1], Arnon Karnieli[3], and Efrat Morin[4]

[1]Centre for Hydrogeology and Geothermics, Université de Neuchtel, Neuchâtel, Switzerland, [2]Department of Hydrology, Geological Survey of Denmark and Greenland, Copenhagen, Denmark, [3]Jacob Blaustein Institutes of Desert Research, Ben Gurion University of the Negev, Be'er Sheva, Israel, [4]Institute of Earth Sciences, Hebrew University of Jerusalem, Jerusalem, Israel, [5]Institute of Earth Surface Dynamics, Université de Lausanne, Lausanne, Vaud, Switzerland

Abstract The quantification of spatial rainfall is critical for distributed hydrological modeling. Rainfall spatial patterns generated by similar weather conditions can be extremely diverse. This variability can have a significant impact on hydrological processes. Stochastic simulation allows generating multiple realizations of spatial rainfall or filling missing data. The simulated data can then be used as input for numerical models to study the uncertainty on hydrological forecasts. In this paper, we use the direct sampling technique to generate stochastic simulations of high-resolution (1 km) daily rainfall fields, conditioned by elevation and weather state. The technique associates historical radar estimates to variables describing the daily weather conditions, such as the rainfall type and mean intensity, and selects radar images accordingly to form a conditional training image set of each day. Rainfall fields are then generated by resampling pixels from these images. The simulation at each location is conditioned by neighbor patterns of rainfall amount and elevation. The technique is tested on the simulation of daily rainfall amount for the eastern Mediterranean. The results show that it can generate realistic rainfall fields for different weather types, preserving the temporal weather pattern, the spatial features, and the complex relation with elevation. The concept of conditional training image provides added value to multiple-point simulation techniques dealing with extremely nonstationary heterogeneities and extensive data sets.

1. Introduction

The small-scale variability of rainfall can sensibly increase the complexity of the hydrological response (Arnaud et al., 2002; Faures et al., 1995; He et al., 2011; Marra et al., 2016b; Segond et al., 2007; Syed et al., 2003; Wilson et al., 1979; Woolhiser & Goodrich, 1988; Yakir & Morin, 2011). A realistic representation of spatial rainfall at the subcatchment scale is crucial to make reliable runoff predictions and forecast extreme hydrological events (Borga et al., 2011). Spatial rainfall fields at the kilometric scale are primarily needed as gridded input to analyze the variability of the hydrological response in space and time. Weather radars provide continuous, high-resolution estimates of the rainfall heterogeneity in space. Being an indirect measure, it is often corrected by comparison with ground measurements (see e.g., Creutin et al., 1988; Hasan et al., 2016; Krajewski, 1987; Sideris et al., 2014; Sinclair & Pegram, 2005; Todini, 1999; Velasco-Forero et al., 2009). Once a radar data set has been proven sufficiently reliable, it can be used as training data set for stochastic rainfall generation. Several stochastic methods are available to simulate an ensemble of rainfall amount fields and study the spatial variability of rainfall. Some techniques perturb the radar-derived fields with a random noise, generated as a multi-Gaussian field correlated to the radar data (Aghakouchak et al., 2010) or showing a more complex covariance structure (Benoit & Mariethoz, 2017; Germann et al., 2009; Kim et al., 2009). A more sophisticated approach is represented by object-based algorithms (Gupta & Waymire, 1979; Northrop, 1996; Paschalis et al., 2013; Russo et al., 2006; Zhang & Switzer, 2007) able to generate new rain fields representing convective environments characterized by isolated rainy objects: the convective cells. The rain cells are simulated as Poisson-point processes (Onof et al., 2000) or using a Markov-chain approach (Peleg & Morin, 2014). Their shape and evolution is then modeled as a random process following parametric statistical laws. Such approach can generate realistic fields but requires a large amount of parameters and,

in some cases, underestimates the extreme values. Among the recent geostatistical techniques, Leblois and Creutin (2013) proposed a model accounting for anisotropy, advection, and turbulence of rain cells and tested it against some reference radar images. Another recent geostatistical method is the dry-drift model (Schleiss et al., 2014), which imposes a deterministic spatial trend that causes the rainfall intensity to augment with the distance from the dry/wet limit. Both works propose as future goal the possibility to introduce nonstationarity in the model conditioned by topographic elevation. This is considered as one primary influence factor on rainfall intensity (see e.g., Hong et al., 2006; Rientjes et al., 2013; Sanchez-Moreno et al., 2014; Yoon & Bae, 2013) and has been already employed as conditioning variable or anisotropy-related factor in geostatistical interpolation techniques for rainfall. Some of them deal with monthly and annual rainfall (Karnieli, 1990; Putthividhya & Tanaka, 2013; Sarangi et al., 2005), for which variogram-based geostatistics, focusing on low-order moments, can be a viable approach since there is not dry-wet pattern and the spatial variability is smooth. A semiparametric interpolation technique based on kernel-smoothing and copula functions has been proposed in Bardossy and Pegram (2013) to assess the marginal distribution of daily rainfall and to relate it with elevation at different locations. This approach allows estimating the full conditional probability density function of rainfall at each point but requires a preprocessing of the elevation data in relation to the wind direction, and the estimation of marginal probability density and copula functions for each day. Moreover, this kind of interpolation treats zero rainfall as censored values without focusing on rain-cell morphology or dry areas.

Another branch of studies, thoroughly reviewed in Fowler et al. (2007), focuses on stochastic generators of weather time series with the goal of preserving the nonstationarity of rainfall events in relation to the synoptic weather characteristics. This type of models finds application in climate downscaling problems. They are usually based on a Markov-chain framework that is conditioned by different types of variables. The conditioning variables include sea level pressure (Corte-Real et al., 1999), temperature and large-scale circulation indexes (Wilby et al., 2002), or upper air pressure (Langousis et al., 2016; Langousis & Kaleris, 2014). These techniques are capable to condition the rainfall statistics using climatic variables without any seasonal analysis. This aspect is convenient to impose seasonal climate change to the simulated data, but they require joint variable transformation, with some limitations where these present complex joint statistics (see e.g., Langousis & Kaleris, 2014). Another approach is to impose the climate conditioning under form of additive or multiplicative change factors on the stochastic model parameters or on the past data (C2SM et al., 2011; Jones et al., 2009; Kilsby et al., 2007). The statistical relation between the synoptic and the rainfall probability density function can also be represented through composite parametric relations, e.g., using generalized linear models (Fealy & Sweeney, 2007; Furrer & Katz, 2007) or generalized additive models (Beckmann & Adri Buishand, 2002; Hyndman & Grunwald, 2000). These techniques may in some cases underestimate the extremes. An alternative way to condition weather generators is weather typing (Hewitson & Crane, 2002; Hughes et al., 1999; Vrac et al., 2007) that makes use of discrete weather states together with climatic predictors in a multivariate Markovian or Bayesian framework. As pointed out in Maraun et al. (2010), this kind of model can lead to complex and intensive calibration involving a large set of parameters. An alternative simulation method is represented by resampling algorithms that can be conditioned by atmospheric indicators (Buishand & Brandsma, 2001; Orlowsky et al., 2008). This data-driven approach tends to produce complex features more easily than parametric techniques but they are more sensible to the availability of training data (see e.g., Oriani et al., 2017).

This study proposes a simulation method that aims at exploring the space-time variability of a given daily weather scenario by stochastic simulation of spatial rainfall amount conditioned by weather indicators and topography. The generation of spatial rainfall fields is based on the direct sampling technique (DS; Mariethoz et al., 2010), belonging to the family of multiple-point statistics (MPS). MPS is based on the concept of training image: a data set that represents the heterogeneity of the variable of interest. This is used to estimate the probability of occurrence of each datum in relation to its neighbors (conditional probability). For rainfall simulation, a training image can be an observed rain event which is considered a valid analogue for the rain field to be simulated. This is the main hypothesis behind the method. In this way, realistic data patterns are generated in the simulation, preserving the high-order spatial dependence in the heterogeneity. To our knowledge, there have been two cases of application of MPS to spatial rainfall simulation. The first one is the simulation of rainfall occurrence (dry/wet pattern) using satellite images to train the algorithm (Wojcik et al., 2009). That application is restricted to the estimation of rainfall occurrence, since the type of

MPS approach used cannot simulate continuous variables. The second one (Jha et al., 2015) is a rainfall and temperature downscaling technique from 50 to 10 km resolution using the Weather Research and Forecasting (WRF) model output images to train the algorithm. The technique preserves the nonlinear statistical relation between temperature and rainfall and it constitutes an efficient alternative to physical downscaling, demanding less computational effort and a simple parameterization. Nevertheless, it is shown that the WRF model output fields, used as training data, present a limited resolution and a tendency to underestimate the extremes (Argueso et al., 2012; Bullock et al., 2014; Caldwell et al., 2009; Zhang et al., 2012).

The methodology presented here uses daily rainfall radar images as training data to simulate high-resolution (1 km) daily rainfall fields conditioned by topographic elevation and daily weather indicators. This is achieved with a novel two-step methodology: (1) the selection of the historical radar images that present weather conditions similar to each day to simulate, the so called conditional training image set (CTIS) and (2) the simulation of daily rainfall field using the associated CTIS as training image set and the digital elevation model as a conditioning variable. This allows estimating the spatial variability of rainfall as a function of the elevation and the daily weather state. With respect to previously mentioned approaches for weather conditioning, the one proposed here is more flexible since it can accommodate continuous or categorical variables with limited parameterization and no specific assumptions on their statistics. The proposed technique can find application for various tasks involving spatial rainfall data. One is to generate multiple rainfall fields for a given historical weather scenario and use it as input of hydrological models to study the uncertainty of subsequent hydrological processes (see e.g., Carpenter & Georgakakos, 2004; Fowler et al., 2005; Renard et al., 2011; Shah et al., 1996). Another possible type of application is the variability assessment of a specific class of rainfall events and their impact (Bonnifait et al., 2009; Duckstein et al., 1972; Zhang & Held, 1999). In this case, only step (2) is applied, with a specific collection of training images. The proposed technique can also be used to simulate gaps in rainfall data sets (data imputation or image-repair techniques; Kim & Pachepsky, 2010; Yang et al., 2005; Wesson & Pegram, 2004) by completing the observed rainfall patterns.

The technique is tested on the simulation of 1 km daily rainfall fields in the eastern Mediterranean during the 2002–2003 wet season. The purpose is to check whether (a) the temporal rainfall variability conditioned by the daily weather state is efficiently represented; (b) if the generated fields present a realistic spatial structure; and (c) if the statistical relation between altitude and rainfall amount is preserved.

The current paper is organized as follows: section 2 describes the data set used, section 3 presents the methodology and the DS setup used, section 4 the evaluation tools. The results are shown in sections 4.1 and 4.2. Section 5 is devoted to the discussion and section 6 to the conclusions.

2. The Data Set

The study area, located in the eastern Mediterranean (Israel and Palestinian Territories), measures 125×124 km^2 (Figure 1). The area is characterized by Mediterranean climate in the central and western parts, arid and semiarid in the southern and eastern parts. The mean annual precipitation ranges from 200 mm in the south to 500 in the north. The south-eastern area is located within a rain shadow and therefore is very arid with less than 200 mm of annual rainfall. The rainfall data used to train and validate the presented technique consists in hourly radar estimates obtained from a non-Doppler, C-Band weather radar (E.M.S. Company) located in the north of the study region (Figure 1). Quantitative precipitation estimates from this instrument have been recently reanalyzed combining physically based corrections and quantitative adjustments based on the comparison with rain gauge measurements of the Israel Meteorological Service network (Marra et al., 2014; Marra & Morin, 2015; Marra et al., 2016a; Peleg et al., 2017). The elaboration procedure takes into account the effects of errors due to antenna pointing, ground echoes, wet radome attenuation, beam blockage, attenuation, and vertical profile reflectivity. Mean field bias and range dependent bias were corrected using rain gauge data. Final radar estimates were converted to 1 km^2 Cartesian grid and accumulated into hourly time intervals. The hourly radar products were created when at least 60% of the expected radar scans were available during the 1 h time interval. The hourly images were then accumulated to 0 A.M. daily time steps.

The historical record used for this study encompasses the periods 1991–1995 and 2001–2005. To condition the rainfall simulation using elevation, the digital elevation model (DEM) provided by the Survey of Israel

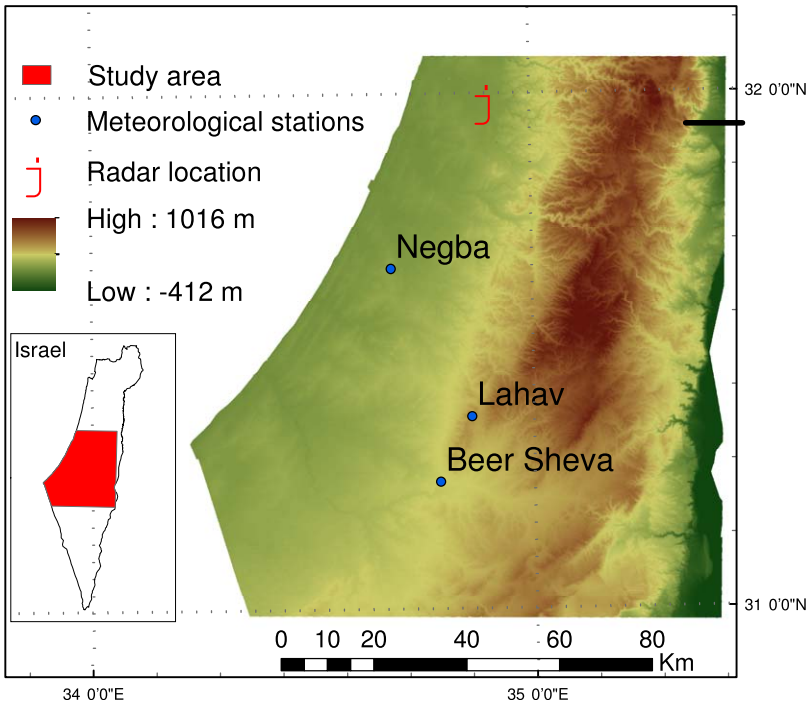

Figure 1. Map of the study area with locations of the radar and meteorological stations used.

has been used. The original 25 m resolution was reduced to 1 km using the nearest-neighbor interpolation technique (Figure 4a). This was preferred than computing the mean over blocks since it allowed a better representation of small-scale features such as minor valleys orientation that can influence the mean rainfall value at lower resolution. As seen from Figure 1, the study region presents a range of altitude gradually increasing from the sea level along the Mediterranean coast on the west to about 1,000 m in the central mountains and rapidly descending to negative values of the Jordan Valley depression (more than 400 m below the sea level). The climate data used were the daily time series of maximum temperature at three ground station located in Beer-Sheva, Lahav, and Negba. The intensity of rainfall events can be statistically linked to the temperature field and climate warming (Berg et al., 2013), also for the Mediterranean (Drobinski et al., 2016) and the study region (Kafle & Bruins, 2009). The daily mean and maximum values were found to have a similar degree of correlation with the total rainfall amount over the study region, but the maximum presented a more exhaustive historical record. For this reason, the daily maximum temperature was chosen among the available climatic variables to characterize the daily rainfall nonstationarity.

3. Methods

The proposed approach generates equally probable realizations of spatial rainfall fields for each time step of a considered daily record. It uses climatic data and an indicator of the weather type, obtained from the analysis of the measured radar data. The technique is composed by two main steps: (1) the selection of radar images from the available historical record and based on the daily synoptic conditions, constituting the conditional training image set (CTIS) and (2) the simulation of a series of daily rainfall spatial fields using the CTIS obtained for each day as training image. Both phases use the direct sampling technique as the core algorithm, but in different ways: in (1), it is used to select images that correspond to similar weather patterns in time; in (2), it is used to generate new rainfall fields by sampling pixels from the training images. In this section, a brief presentation of the direct sampling method is given, then the methodology proposed is described in detail.

3.1. The Direct Sampling Technique

MPS techniques are usually applied for the stochastic simulation of complex heterogeneities, where low-order-moment characterization is not sufficient to properly catch the spatial variability. MPS algorithms generally analyze the probability of occurrence of each event with respect to the data patterns found in the

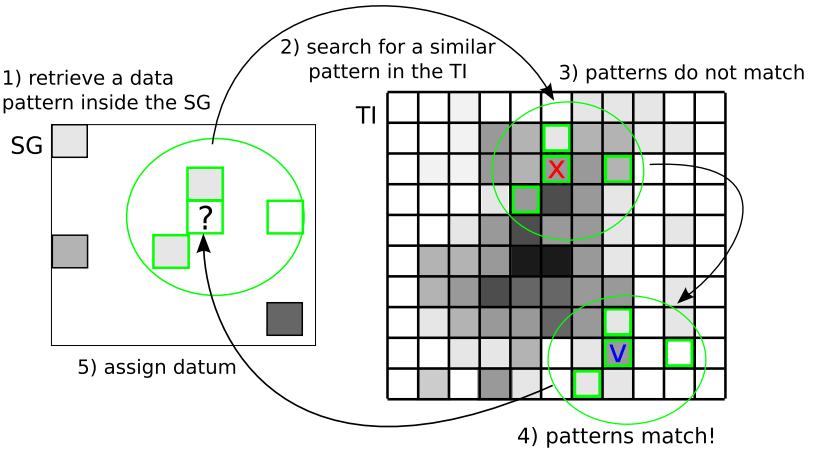

Figure 2. Sketch of the direct sampling iterative workflow in the two-dimensional simulation of a continuous variable, illustrating the generation of one value in the simulation grid (SG) by resampling from the training image (TI).

training image (TI), representative of the simulated variables. In this way, high-order statistical dependencies are taken into account and the simulated data preserve many of the geometrical and topological features present in the TI. Direct sampling (DS) is an MPS algorithm that randomly scans the TI until a similar pattern is found. The value at its center is assigned to the simulated location, without computing any probability measure (see the sketch in Figure 2).

The DS implementation used in this paper, called *DeeSse* (Straubhaar, 2011), allows the simulation of multiple variables at the same time. It can be used to simulate either time series (section 3.2) and spatial variables (section 3.3). The following is the main workflow of the algorithm for spatial simulation. In the case of time series simulation, all variables are time referenced and unidimensional. For more details and a comparison with other resampling techniques, see Oriani et al. (2014). The simulation follows a random path which visits a space referenced empty array **X** called simulation grid (SG), that becomes progressively populated until the target variable $K(x)$ is simulated at all locations. The values are generated by sampling with replacement the TI **Y**, composed of historical radar images and auxiliary variables. The simulation proceeds as follows:

1. Select a random location x in the SG that has not yet been simulated.
2. To simulate $K(x)$ (e.g., the rainfall amount at the location x): retrieve a data event $\vec{d}(x)$, i.e., a group of already simulated or informed neighbors of x, according to a fixed circular spatial window of radius R. $\vec{d}(x)$ consists of at most the N informed locations closest to x inside the mentioned window. The size and configuration of $\vec{d}(x)$ is therefore limited by the user-defined parameters N and R, and the number of already informed neighbors inside the considered window. If no neighbor is informed, e.g., at the beginning of a simulation with no conditioning data, $\vec{d}(x)$ results to be empty.
3. Visit a random location y in the TI. If $\vec{d}(x)$ is empty, assign the value of $K(y)$ to $K(x)$ and repeat the procedure from the beginning. Otherwise, retrieve the corresponding data event $\vec{d}(y)$.
4. Compute a distance $D(\vec{d}(x), \vec{d}(y))$, i.e., a measure of dissimilarity between the two data events. For categorical variables (e.g., the dry/wet rainfall sequence), the proportion of nonmatching elements of $d(\cdot)$ is used as criterion, while for continuous variables the choice is the mean absolute error.
5. If $D(\vec{d}(x), \vec{d}(y))$ is smaller than a fixed threshold T, assign the value of $K(y)$ to $K(x)$. Otherwise repeat from step 3 to step 5 until the value is assigned or a prescribed TI fraction F is scanned. T is expressed as a fraction of the total variation shown by K in the TI. For example, $T = 0.05$ allows $D(\vec{d}(x), \vec{d}(y))$ up to 5% of the total variation. In case of a categorical variable, $T = 0.05$ allows a mismatch between $\vec{d}(x)$ and $\vec{d}(y)$ for 5% of the composing neighbors.
6. If the prescribed TI fraction F is covered by the scan, assign to $K(x)$ the scanned datum $K(y^*)$ that minimizes D among the visited candidates.
7. Repeat the whole procedure until all the SG is informed.
8. The simulated field ensemble is back-transformed using a quantile-quantile transformation toward the empirical cumulative distribution of the TI. This operation assures the preservation of the distribution tail in case of extremely rare events present in the training data set.

The same process is applicable to a multivariate data set, where k variables $K(x, k)$ are simulated. The parameters N_k, R_k, and T_k allow defining different pattern dimensions and acceptance threshold for each kth variable. Conditional data for the target variable are admitted and treated as already simulated data. Conversely, any missing conditional variable is simulated as target variable. This allows using incomplete conditioning data sets. The DS technique relies on the following parameters: the maximum scanned TI fraction $F \in (0, 1]$ at each scanning iteration, the search neighborhood radius R, the maximum number of neighbors N, both expressed in number of pixels, and the distance threshold $T \in (0, 1]$. Apart from F, each parameter is set independently for each simulated variable, allowing different size for the conditioning data patterns.

3.2. Step 1: Generating the CTIS

To apply the proposed method, a first requirement is to have a representative stack of daily radar images to be used as training image. Since the features contained in such data records can be extremely nonstationary, it is not appropriate to use the whole radar data set to train the algorithm for the simulation of different weather types. Therefore, the first step is the characterization of the nonstationarity observed in the data set and the stochastic selection of an appropriate subsample of images for each day of the simulated climatic scenario. This was done with the help of auxiliary variables. The historical data set was treated as multivariate daily time series including: the annual seasonality described by $A1$ and $A2$, the weather type C, the maximum daily temperature at three stations $S1$, $S2$, and $S3$, and a pointer to the daily radar image P. As shown by the sketch in Figure 3, DS was used with this data set to select a series of radar images for each day of the simulated weather scenario. This process has the form of a multivariate time series simulation where the historical record was used as training image (TI), and the daily time line of the simulated scenario was the simulation grid (SG). All the auxiliary variables ($A1$, $A2$, $S1$, $S2$, $S3$, and C) were known for the weather scenario, while P was the simulated variable redirecting to the historical radar images. In particular, $A1$ and $A2$ are wave functions computed on the daily time line and giving information about the position in the year. Both functions have period τ=365.25 days to compensate for leap years, a reciprocal phase shift $\theta=\tau/4$, and triangular shape. $(A1, A2)$ allows identifying the position of each day in the year with a continuous variation, to preserve the nonstationarity linked to the annual seasonality. C indicates the weather type, based on a simple analysis of the radar images explained in the following. The rainy weather types in the study region can be broadly divided into two categories: (1) relatively common rain events caused by Mediterranean cyclones, that tend to spread over the north-west part and (2) rare and more localized events in the southern-eastern part. This category may be linked to Mediterranean cyclones or to the phenomenon of the Active Red Sea trough, a depression in the surface pressure field extending from eastern Africa along the Red Sea toward the Middle East (see e.g., Kahana et al., 2002; Tsvieli & Zangvil, 2005). These classes of events present extreme daily rainfall amounts over 100 and 50 mm, respectively. To apply this classification, the radar images were divided into two subregions by tracing the SW-NE diagonal: the north-west (NW) and the south-east (SE). The mean daily rainfall intensities for the whole image ($\hat{r}$) and the two subregions ($\hat{r}_{NW}$ and $\hat{r}_{SE}$), were computed. Also the sixth and ninth quantiles of the total ensembles $\{\hat{r}_{NW}\}$ and $\{\hat{r}_{SE}\}$ were computed ($Q_{.6NW}$, $Q_{.6SE}$, $Q_{.9NW}$, and $Q_{.9SE}$). This allowed the definition of the variable C describing the weather type and intensity for each day (Table 1). The choice of the quantiles to classify the event intensity was in this case arbitrary: $Q_{.9}$ is a usual threshold for high-intensity events, while $Q_{.6}$ corresponds approximately to the midrange of the values lower than $Q_{.9}$ for both NW and SE events. More characteristic values may be found, e.g., by putting in relation the rainfall amount to the hydrological response of the studied catchment.

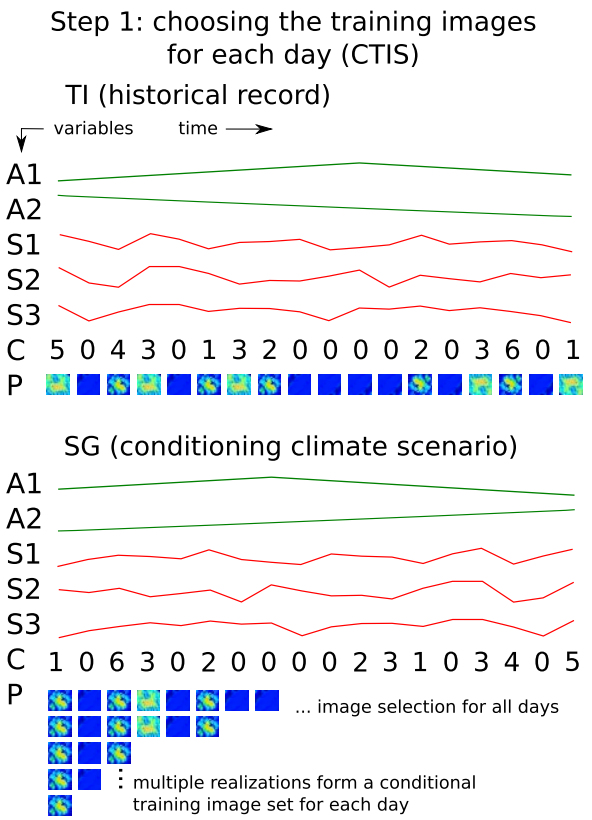

Figure 3. Sketch of the technique used to select the conditional training image set for each day of the conditioning weather scenario, using the historical record as training image (TI). The variables used are indicated with capital letters.

The DS parameters (see section 3.1) were set up as follows. For variables $A1$ and $A2$ no multiple-point conditioning pattern was used since the variables are deterministic and define univocally the position of each day in the calendar. For this reason, the search neighborhood radius (R) and maximum number of

Table 1
Definition of the Values Taken by the Variable C *That Classifies the Daily Weather Type*

C value	Condition met	Description
0	$\hat{r} > 0.2$ mm	Dry weather
1	$\hat{r} > 0.2 \wedge \hat{r}_{NW} > \hat{r}_{SE} \wedge \hat{r}_{NW} \leq Q_{.6NW}$	Weak NW event
2	$\hat{r} > 0.2 \wedge \hat{r}_{SE} > \hat{r}_{NW} \wedge \hat{r}_{SE} \leq Q_{.6SE}$	Weak SE event
3	$\hat{r} > 0.2 \wedge \hat{r}_{NW} > \hat{r}_{SE} \wedge Q_{.6NW} < \hat{r}_{NW} \leq Q_{.9NW}$	Moderate NW event
4	$\hat{r} > 0.2 \wedge \hat{r}_{SE} > \hat{r}_{NW} \wedge Q_{.6SE} < \hat{r}_{SE} \leq Q_{.9SE}$	Moderate SE event
5	$\hat{r} > 0.2 \wedge \hat{r}_{NW} > \hat{r}_{SE} \wedge \hat{r}_{NW} > Q_{.9NW}$	Strong NW event
6	$\hat{r} > 0.2 \wedge \hat{r}_{SE} > \hat{r}_{NW} \wedge \hat{r}_{SE} > Q_{.9SE}$	Strong SE event

Note: Each category corresponds to a specific range of the mean daily rainfall intensity ($\hat{r}$) and relation between the same quantity measured in the south-eastern ($\hat{r}_{SE}$) and north-western ($\hat{r}_{SE}$) portions of the study zone. Q_n indicates the n-quantile computed either on $\hat{r}_{SE}$ or $\hat{r}_{NW}$.

conditioning neighbor data (N) were set to 1. The distance threshold (T) was set to 0.1, meaning that 10% of variation on the day of the year (more than 1 month) was allowed when looking for a radar image to assign the current day. This value allows enough flexibility to simulate a change in the seasonality imposed by the other conditioning variables. For the maximum temperature time series ($S1$, $S2$, and $S3$), the conditioning pattern was formed by the closest 15 neighbor data ($N = 15$) in both past and future. For the weather category C, the conditioning neighborhood was restricted to two neighbors ($N = 2$), to preserve the lag-1 time dependency in the succession of weather types. For variables $S1$, $S2$, $S3$, and C, the distance threshold T was setup to 0.05 (5% of the total variation) according to previous DS applications to rainfall and climate variables (Oriani, 2015; Oriani et al., 2014). Finally, the parameters for P were set to 1, since the variable only contains pointers to the radar images without any significant temporal dependency. Following previous DS applications, F was set to 0.5, meaning that up to 50% of the TI was scanned at each DS iteration. This value, in line with the setup of previously mentioned DS applications, is established by trial and error usually between 0.3, for extensive and rather stationary training data set, and 0.5, for limited or nonstationary training data sets. Increasing the maximum percentage of scanned data set can lead to the reproduction of large portion of training data (verbatim copy, see Oriani et al., 2014).

The workflow was repeated to select a set of 100 images for each time step, forming the daily CTIS. Note that the TI was scanned each time in a random order and an image could be selected multiple times for the same day, for example, in case of rare weather conditions. This process allows preserving the weather variability according to the probability of occurrence of the corresponding climatic conditions.

3.3. Step 2: Generating the Daily Rainfall Fields

Once the CTIS for each day has been selected, a series of spatial rainfall fields was simulated using DS. In this phase, the simulation was only spatial, with no explicit temporal dependency in the simulated fields, although the CTIS used follows the temporal daily weather pattern imposed by the conditional variables (section 3.2). The rainfall amount K (mm), from radar images, was simulated together with two auxiliary variables computed from the same data (we simplify the notation by omitting the space reference (x)): (1) the elevation M (m) was completely informed in the SG and given as conditioning data and (2) W, a categorical variable describing the dry/wet and extreme-value pattern (0 if $K \leq 0.2$ mm, 1 if $0.2 < K \leq Q_{0.9}$ and 2 if $K > Q_{0.9}$, where $Q_{0.9}$ is the 0.9-quantile of K measured on the current CTIS). W was cosimulated with K. An example of one radar image together with the auxiliary variables used is given in Figure 4. Since the correlation length of the observed rainfall structure is longer than the domain size, the search window radius R was set to 60, so that the window covers almost the entire TI. $N = 10$ for all variables and $T = 0.05$ for M while it was set to 0.002 for W and K. These parameters were set following the results of a previous sensitivity analysis for daily rainfall time series (Oriani, 2015), in line with previous analysis on other heterogeneities (Meerschman et al., 2013). These studies show that R should take a value larger than the correlation length of the simulated structures, while no precise relationship between the parameters N and T and the physical or statistical properties has been established yet. Nevertheless, it has been observed that the appropriate parameter set converges to a unique solution that is appropriate for different climate settings (Oriani et al., 2014). For the spatial heterogeneity simulated in this paper, the distance threshold (T), usually varying in [0.01–0.010], was set about 1 order of magnitude lower than the value used for daily rainfall time series. The

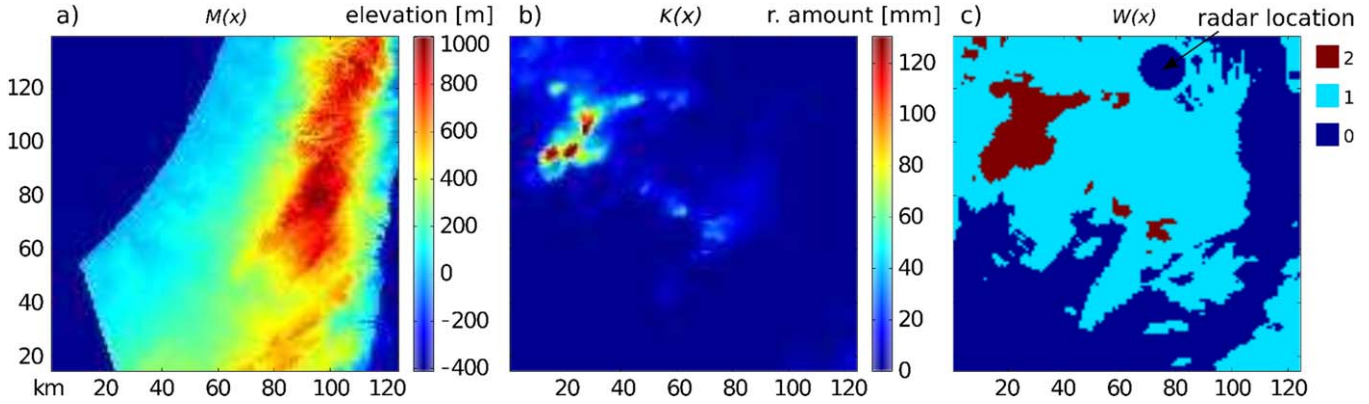

Figure 4. One example of daily spatial variable used in step 2 of the simulation technique: (a) elevation $M(x)$, (b) daily rainfall amount K, and (c) dry/wet/extreme categorical pattern W. The circular zone indicated by the arrow in Figure 4c is a missing data region surrounding the radar station.

motivation is that, considering a resolution of 1 day and 1 km, the rainfall amount is much more correlated in space than in time: the spatial variation is smoother and requires a stricter rule for pattern acceptance to avoid adding excessive small-scale noise brought by the resampling procedure. N, taking integer values usually in the range [1,50], and can be manually setup by trial an error. Complex heterogeneity requires higher N values. The parameter F was set to 0.5, so that maximum 50% of the pixels inside the daily CTIS was scanned at each DS iteration.

4. Evaluation

To test the proposed methodology, two experiments were carried out: a preliminary one (section 4.1) analyzing the stationary simulation of two specific types of events and a second one (section 4.2) testing the entire workflow to generate rainfall fields conditional to a weather scenario. The simulated rainfall fields were visually compared with the reference ones and a series of statistical indicators were computed as follows. The empirical joint probability density function (JPDF) was used to analyze the statistical relation between elevation and rainfall amount. After computing the cumulative JPDF and normalizing this to sum up to one, the percentage overlap (see histogram interception; Swain & Ballard, 1991) was computed on this distribution. To analyze more in detail the statistical relation between topography and rainfall amount, the rainfall amount-slope orientation JPDF is computed on the reference and generated rainfall fields in the second experiment, together with the slope orientation map. This allows illustrating the orographic effect on the spatial distribution of the rainfall amount. The slope orientation is obtained by computing the gradient direction on the digital elevation model. Moreover, the experimental variogram was used to analyze the covariance structure of the fields and their variability at different scales. To estimate the variogram on a sufficient number of points, all the available pixel couples in the N-S and E-W directions were considered, respectively. Areas located in the neighborhood of the radar apparatus, in a radius of approximately 20 km and up to 50 km eastward, were excluded from the computation since they present artifacts that alter the covariance estimation. In the second experiment, the time series of daily mean rainfall and wet area fraction over the entire field were compared to check whether the temporal pattern of the considered weather scenario is preserved in the simulation.

To test whether the simulated variability in the time series is reliable, we introduced an indicator called the *average quantile interval mismatch*: B. It quantifies whether a reference time series falls with the right probability within the interval defined from an ensemble of simulations. To define it, let us introduce K_t, with $t=1,\ldots,G$, a reference time series of a quantity such as the total daily mean rainfall over the rainfall field, wet area percentage, or any other quantity of interest. This is the reference against which one wants to compare the simulations. It is usually not available for future forecasts, but for testing the technique we use a past reference record. The simulation procedure produces a set of stochastic realizations of rainfall fields from which we derive the estimate ensemble $\{\hat{K}_t\}$ for every time step t. From this ensemble of time series, one can estimate, for each time step t, the quantiles $\hat{K}_t^p$, so that the probability measure $P(\hat{K}_t \leq \hat{K}_t^p)=p$, with $p \in [0,1]$. Similarly, the time-varying interquantile range $[\hat{K}_t^{p_1}, \hat{K}_t^{p_2}]$ defines the interval in which $\hat{K}_t$ falls

with probability (p_2-p_1) at each time step. The reference time series K_t should fall within this interval with the same probability, if the variability is correctly estimated by the simulation ensemble. We then define an indicator variable that is equal to 1 when the reference falls within an interquantile range $[\hat{K}_t^{p_1}, \hat{K}_t^{p_2}]$, with $p_2 > p_1$.

$$\mathbb{I}(p_1, p_2, t) = \begin{cases} 1 & \text{if} \quad \hat{K}_t^{p_1} \leq K_t \leq \hat{K}_t^{p_2} \\ 0 & \text{otherwise} \end{cases} \tag{1}$$

In the last step, all the information is aggregated in time by comparing the empirical probability of $\mathbb{I}(p_1, p_2, t)=1$ with the probability of the quantile interval $[\hat{K}_t^{p_1}, \hat{K}_t^{p_2}]$:

$$B_{p_1,p_2} = \left[\frac{1}{G}\sum_{t=1}^{G} \mathbb{I}(p_1, p_2, t)\right] - [p_2 - p_1] \tag{2}$$

B_{p_1,p_2} is a function of $(p_1, p_2, K_t, \hat{K}_t)$ taking values in $[-1, 1)$. For example, considering the quantile range $[\hat{K}_t^{0.1}, \hat{K}_t^{0.9}]$, K_t should lie within this interval 80% of the days. In that case, $B_{p_1,p_2}=0$. Positive values of B correspond to the reference lying too often inside the quantile interval, indicating a tendency to overestimate the daily variability. Conversely, negative values correspond to the reference lying too often outside the quantile interval, corresponding to underestimation of this variability (quantile interval too narrow) or systematic bias (quantile interval shifted with respect to the reference). In this study, we considered the 0.05–0.95-quantile boundary to analyze the variability in the previously mentioned time series of mean rainfall and covered area. Due to the extreme nonstationarity of these quantities, it is reductive to compare the marginal distributions of the time series. On the other hand, average error measures do not evaluate whether the estimated variability is properly assessed. In this cases, the indicator B is more appropriate since it is robust to nonstationarity and focuses on the simulation ensemble confidence boundaries instead of the average predicted value.

In addition, the efficiency in preserving the variability of the rain-cell characteristics was analyzed by computing the histogram of the rain-cell mean rainfall amount, covered area and orientation. For this purpose, the daily rainfall fields were converted into binary images by putting the rainfall amount lower than 0.2 mm to 0 and the rest of the field to 1, according to the dry/wet classification of the simulation setup (section 3.3). The obtained binary fields show the rain cells as connected components, allowing the computation of the mentioned indicators. The orientation analysis was restricted to rain cells of size larger than 10 pixels (10 km^2), to focus on the main asymmetry and orientation of the rainfall fields.

4.1. Stationary Simulation

This preliminary experiment was performed using two groups of 30 radar images showing respectively the NW and SE event types of average and high intensity described in section 2. The number of images is dictated by the availability of observed events, in particular of SE type. Each group shows images that are not in temporal continuity but constitute a catalog of rainfall fields showing a similar heterogeneity. The aim of this test is to analyze the efficiency of the proposed technique in simulating a stationary set of rainfall fields without any conditional climate variables, by only applying step 2 (section 3.3) of the proposed methodology. The simulation was repeated 10 times (10×30 images generated for each weather type), to analyze the extremal behavior of the simulated process with return time events observable in the reference. The TI was also used as reference and compared with the simulated fields. The results are shown in the following.

Figures 5a and 5d show one example of the reference and simulated fields for rainfall events from NW and SE, respectively. The simulated fields show a realistic range of values and spatial structures. The rainfall intensity inside the rain cells follows the dry drift (Schleiss et al., 2014) similarly to the reference. Extended events from NW (Figure 5a) spread over a wide region and show a smooth transition from low to high values, while the events from SE (Figure 5c) show an abrupt transition to local maxima and less spatial continuity, with occasional occurrence of isolated rain cells in the NE. The simulation mean shows that the expected covered area is preserved for both types of events. The simulation shows rather similar characteristics, including the main orientation and connectivity, although a moderate small-scale noise is visible. This phenomenon is linked to the sampling process that aims at preserving on average multiple-data patterns without focusing uniquely on pixel-to-pixel transition.

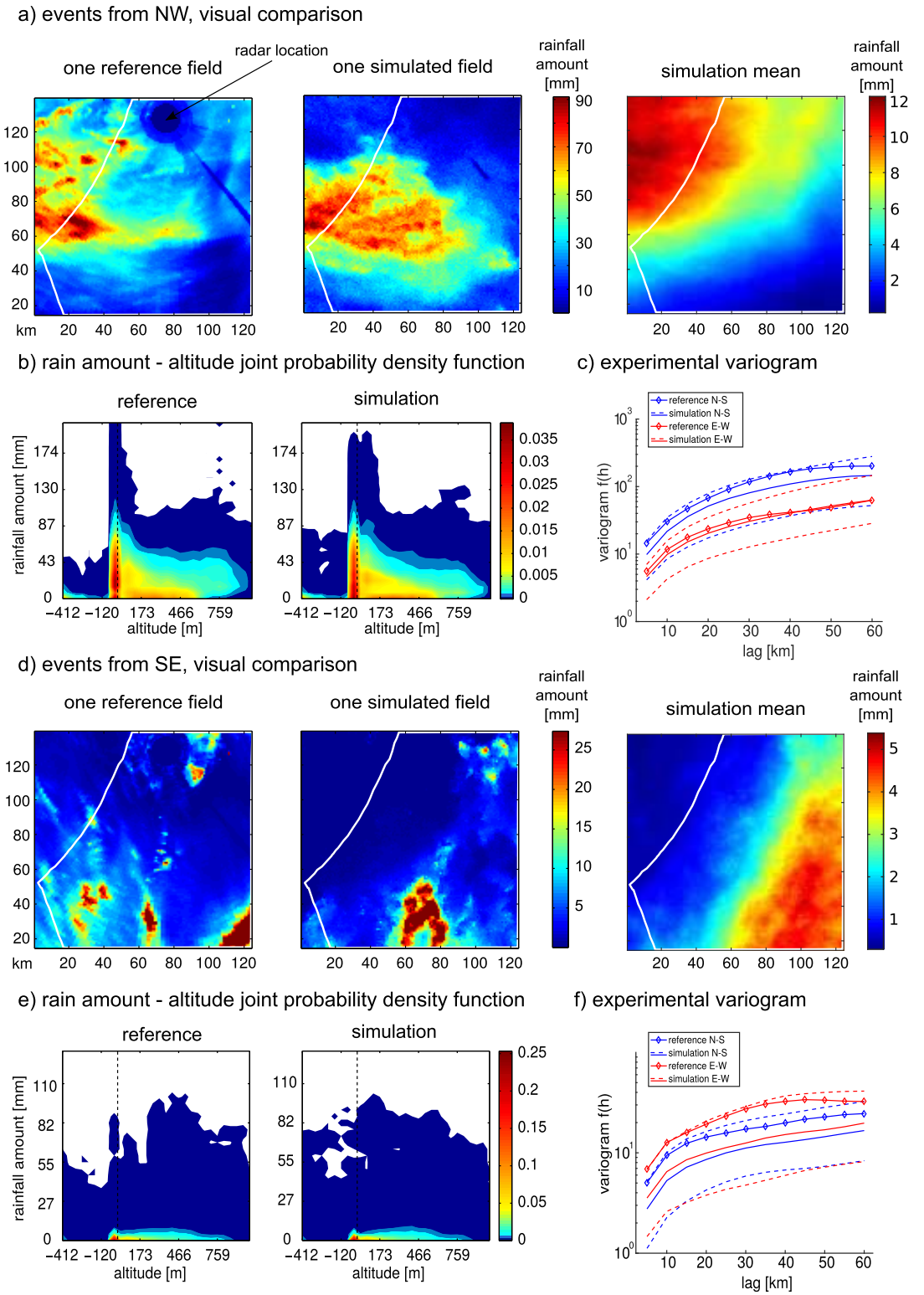

Figure 5. Results of the unconditional simulation of two groups of images representing events from NW and SE, respectively: (a, d) visual comparison of the rainfall fields, (b, e) rain amount-altitude joint probability density function, and (c, f) experimental rainfall amount variogram for the N-S and E-W directions. In Figures 5a and 5b, the white line represents the shore line and study region perimeter. In Figures 5b and 5e, the dashed line indicates the 0 m altitude. In Figures 5a and 5d, the simulation mean is computed on the whole simulation ensemble (10×30 fields). In Figures 5b and 5e, the joint probability density function is computed on 30 random fields (the same number of the reference). In Figures 5c and 5f, the dashed line indicates the variogram computed the 0.05–0.95-quantile boundaries of the simulation ensemble, the continuous line indicates the median of the realizations, and the dotted line is the reference variogram.

For both field types, the rain amount-altitude JPDF (Figures 5b and 5e) is accurately preserved in the simulation. Note that this indicator was computed on the 30 reference and random simulated images, to keep the same amount of data. The core of the rainfall distribution, the extremal part, showing extreme rainfall events with near-zero probability of occurrence, as well as the complex relation with altitude are well represented. In particular, the complex nonstationarity is preserved by generating realistic multivariate altitude-rainfall data patterns, instead of building a complex parametric model for the joint spatial correlation of the two variables. Different areas of the study zone are associated with a specific rainfall distribution: negative altitude values correspond to the Jordan Valley in the east, with scarce rainfall occurrence, near-zero values correspond to the western coastal zone with the more frequent and extreme events, while the positive altitude values correspond to the highlands and mountainous regions with lower extremes.

Finally, the rainfall amount variogram of the simulated fields (Figures 5c and 5f) shows a central tendency, indicated by the median of the realizations (central line), in good agreement with the reference and a variability of the simulation ensemble that spans over 1 order of magnitude. Both short-distance and long-distance correlations are preserved accurately for the events from NW, while there is a more marked tendency to underestimate the variability for the events from SE. This may be due to the higher nonstationarity of these fields that makes the variogram highly sensible to the occurrence of concomitant rain cells at different distances. In these cases, a larger training image may allow a better preservation of the variogram.

4.2. Nonstationary Simulation Conditioned by a Weather Scenario

This second experiment sees the application of the entire proposed methodology: the CTIS selection (step 1, section 3.2) and the rainfall-field simulation (step 2, section 3.3). The CTIS selection was conditioned by the weather scenario observed in the season 2002–2003, using the 1991–1996 historical record as TI. Then, a series of 10 rainfall fields was simulated for each day. The results were analyzed using the 2002–2003 radar record as reference. This wet season presents a high number of rainy days, allowing testing the technique over several different rainfall events. Similarly to the previous test, two main classes of events were considered for comparison with the reference: the NW and SE events. The simulated period is composed of 231 days, including 90 NW events, 5 SE events, and 136 dry days. The SE events are rare and the computed statistics may be less representative for this class.

Figure 6 shows the time series of the daily mean rainfall and wet area coverage over the entire simulated period: the simulation ensemble follows the reference temporal pattern quite accurately. This result suggests the efficiency of the weather classification used to condition the CTIS selection of step 1 (section 3.2), i.e., the technique allows the choice of the appropriate training images in the historical record on the basis of the information about the daily temperature and weather. The variability is larger for strong rain events and both indicators and the reference is mainly included within the ensemble boundaries. Weak rainfall events presenting a low mean rainfall value but a large covered area are also represented in the simulation. The *average quantile interval mismatch* $B_{0.05,0.95}$ (see section 4) is of 0.0028 for the mean daily rainfall and 0.0004 for the wet area coverage, suggesting that the simulated variability is realistic with respect to the reference time series.

Figure 7 provides a visual comparison between the reference and three simulated fields of both classes. Note that the simulations are conditioned in space by elevation only, so they do not aim at representing the exact reference field. However, they should preserve a similar type of heterogeneity since they are conditioned by the same daily weather information. Similarly to the preliminary test results (section 4.1), the simulated fields present a realistic internal structure, shape and location of the rain cells. The average amount computed on the simulation ensemble shows that the main rainfall accumulates on the NW for the first class and SE for the second, honoring the weather type. The average rainfall shows that the NW events are more intense than the SE events and cover a wider area, with maxima along the Mediterranean coast and central mountainous region. The standard deviation shows, for both classes, an irregular variability pattern, linked to the position of the simulated maxima.

The rainfall amount-altitude JPDF and variogram of the fields (Figure 8) confirm the efficiency of the technique in preserving the complex relation among altitude and rainfall amount, and the overall spatial variability of the fields. In both cases, the reference and simulation cumulative JPDF overlap (see section 4) is 98.8% for the NW type and 99.6% for the SE type of events, confirming that the distribution is mainly preserved. The JPDF was computed considering all the observed days for the NW and SE classes, and one random simulated image per day, to compare the same amount of data. The simulation produces higher

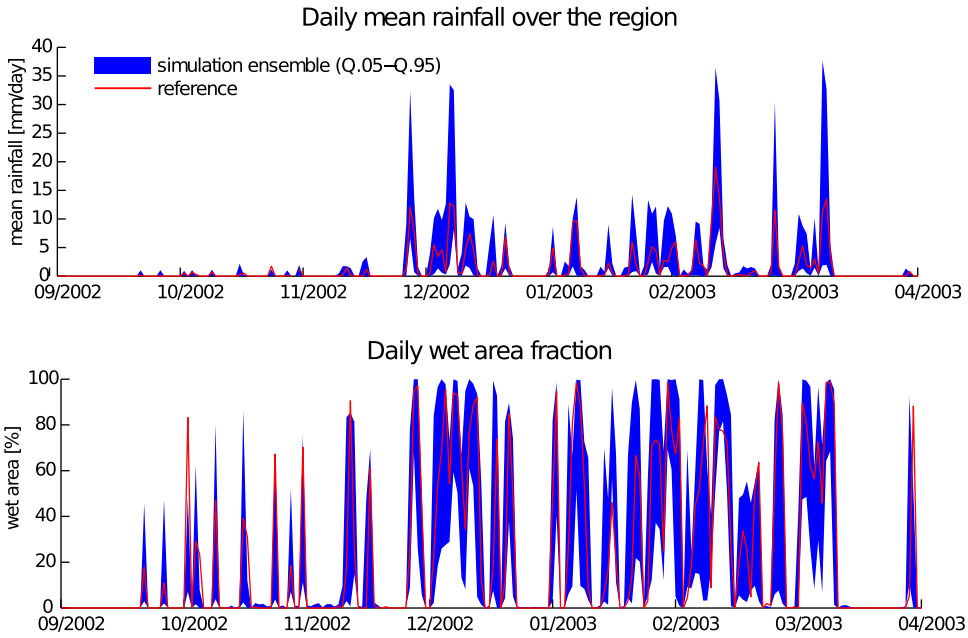

Figure 6. Time series of the daily mean rainfall and percentage of the field area covered by rainfall in the simulated period. The red line indicates the reference and the blue area the range of values within the 0.5–0.95-quantile boundary of the simulation ensemble.

extremes than the ones observed in the reference JPDF for SE events (Figure 8b). This is due to the fact that the CTIS used, issued from the historical record, shows larger variability than the reference fields for this class of events. This also confirms the need of exploring the variability through ensemble simulation in addition to the sole analysis of the radar images available for the period of interest.

Figure 9 provides the analysis of slope orientation in relation to the rainfall amount probability distribution. The slope orientation map (Figure 9a) shows that the spatial distribution of the slope orientation in the study region is nonstationary: the western slope of the central mountains shows the positive slope increment angle mainly varying in [0,–50] degrees from E-W (red color). In other words, the slope is directed toward W-NW, perpendicularly to the coast line. Conversely, the eastern slope is mainly directed towards E-SE (green color). The rainfall amount-slope orientation JPDF (Figures 9b and 9c) shows that, for both NW and SE events, rainfall is more frequent and intense for the slope orientation range [0,–50], mainly corresponding to the eastern slope of the central mountains, exposed to the rainfall events coming from the Mediterranean. This probabilistic structure is fairly well preserved in the simulated fields, indicating that the orographic effect on rainfall is represented in the simulations. Also in this case, the reference and simulation cumulative JPDF overlap is 98.8% for the NW type and 99.6% for the SE type of events.

Similarly to the analysis conducted in Peleg and Morin (2012), the morphology of the rainfall fields was analyzed by comparing the histogram of the rain-cell mean rainfall, area, and orientation (Figure 10). For NW events, the rain amount and area frequency distribution is preserved for all indicators up to the extremes, but rain cells presenting weak mean rainfall (0–2 mm) and small area (1–4 km^2 equivalent to 1–4 pixels) are overrepresented. This phenomenon is probably linked to the small-scale noise created in the simulation, mentioned in section 4.1. The rain-cell orientation distribution, showing a preferential E-W orientation, is accurately preserved.

The computation of these indicators for the SE type of events is less representative, due to the low number of reference fields. Rain cells seldom present a rainfall amount higher than 2 mm in both the reference and simulated fields. Large covered areas up to 15,000 km^2 occur rarely in the reference and they are moderately underrepresented in the simulation. The reference shows a preferential NS orientation that is not captured in the simulation. The mean rainfall measured in the study region and cumulated over the reference record is of 283 mm, while the simulation ensemble shows values between 195 and 414 mm (0.05–0.95-quantile range), with a median of 311 mm.

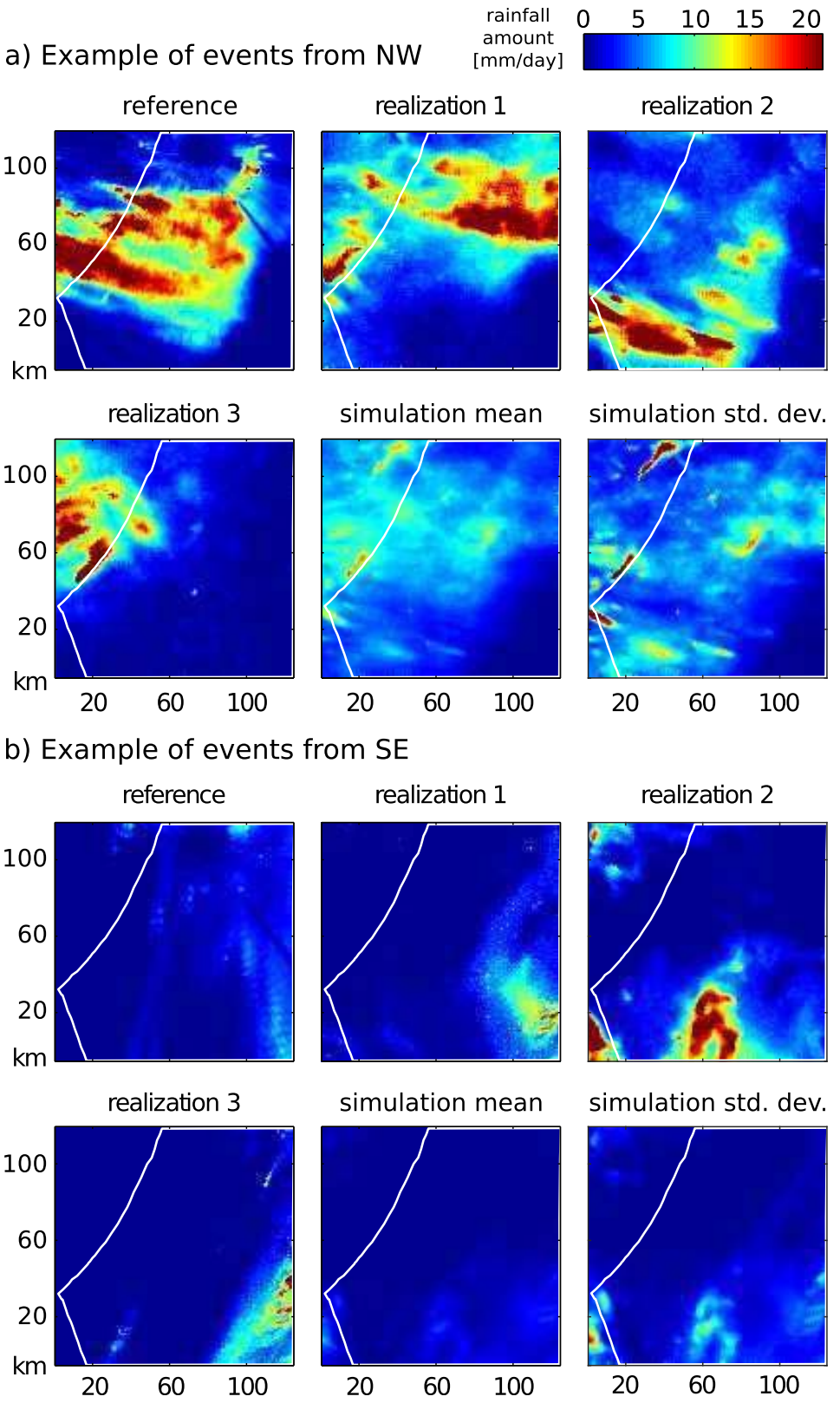

Figure 7. Visual comparison of the daily rainfall fields for the (a) NW and (b) SE classes. For both Figures 7a and 7b, one daily reference field is shown together with three simulated fields, the mean and standard deviation of the simulation ensemble for the reference day. The white line represents the shore line and study region perimeter.

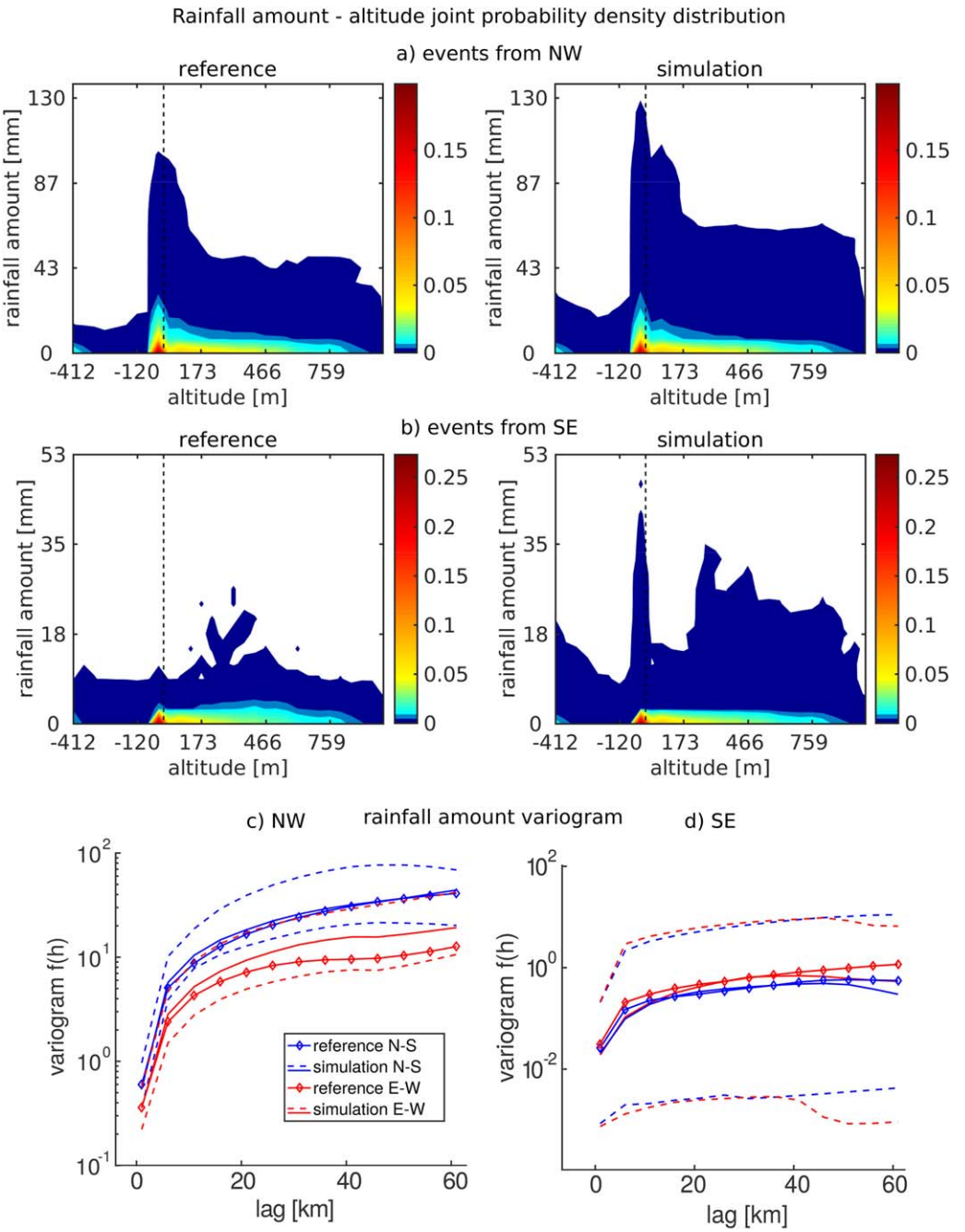

Figure 8. Rainfall amount-altitude joint probability density function and variogram computed for the N-S and E-W directions on the reference and simulated fields for the (a, c) NW and (b, d) SE classes, respectively. In Figures 8a and 8b, the dashed line indicates the 0 m altitude. In Figures 8c and 8d, the dashed line indicates the variogram computed the 0.05–0.95-quantile boundaries of the simulation ensemble, the continuous line indicates the median of the realizations, and the dotted line is the reference variogram.

5. Discussion

The presented simulation technique allows a realistic variability analysis by simulating spatial rainfall amount conditioned by elevation, temperature, and weather type, with minimal parameterization. By making multiple realizations, the technique can give a full conditional probability distribution estimation of rainfall at each point, a goal that is difficult to achieve and usually requires complex statistical models (see e.g.,

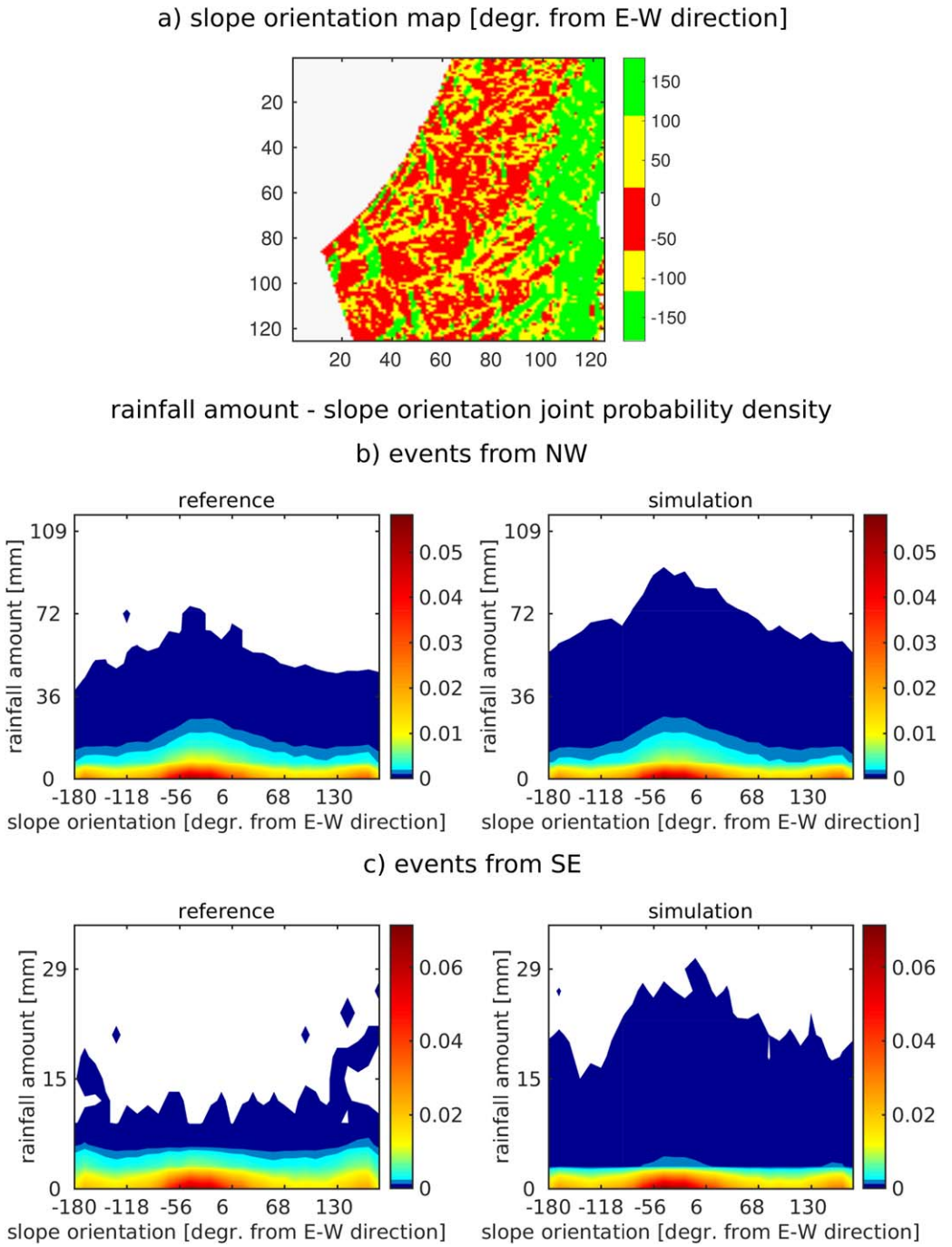

Figure 9. (a) Slope orientation map and rainfall amount-slope orientation joint probability density function for the (b) NW and (c) SE.

Bardossy & Pegram, 2013). Moreover, the technique produces conditional rainfall fields that can be used as input data to propagate the variability to hydrological models.

The technique can represent the statistical relation with elevation to a high degree, as shown not only by the point-to-point JPDF, but also by the relation between slope orientation and rainfall amount. This is achieved by considering multiple-point and multiple-scale patterns of elevation and rainfall amount, carrying implicit information about the morphology and orientation of the topography. Although further tests

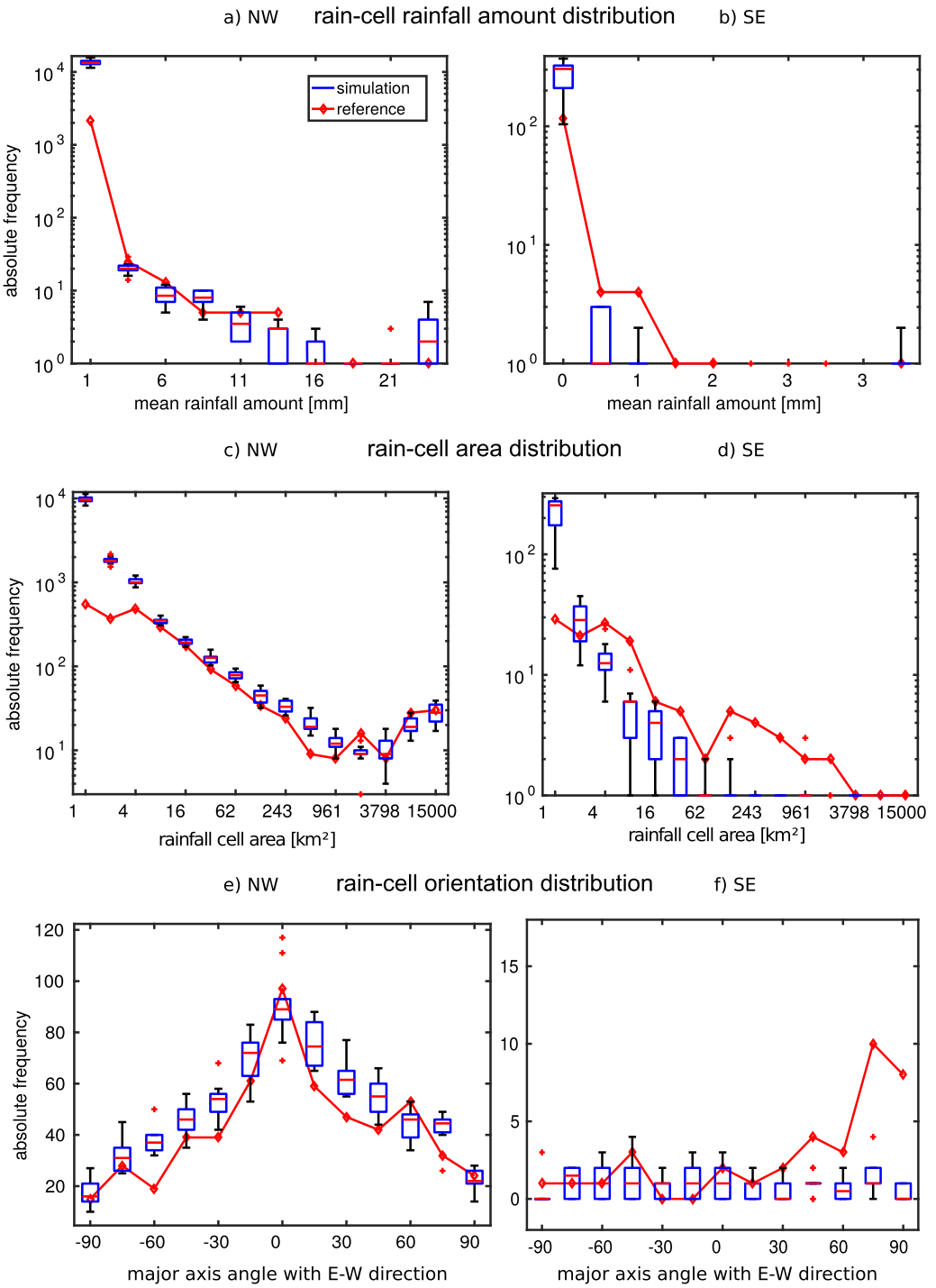

Figure 10. Histogram of the (a, b) rain-cell mean rainfall amount, (c, d) covered area, and (e, f) orientation for NW and SE classes. The red line indicates the reference and the box plots represent the simulation ensemble.

should be carried on, this setup is in principle adaptive to other terrains, using the only information contained in the two mentioned variables.

The morphological analysis of the rain-cell intensity, area, and orientation shows that these features are mainly preserved in the simulations, even if they are not parametrized in the algorithm. The preservation of these high-order features leads to a more realistic representation of the spatial variability than the parametric approaches based on the estimation of low-order moments (see e.g., Schleiss et al., 2014). Nevertheless,

it is fundamental to use a representative training record, since the algorithm should dispose of a large series of similar data patterns. Indeed, the results show that the estimation of the rain-cell features is less precise in the case of weather states which are rare, thus poorly represented in the training images. This limitation, existing to different extent for both parametric and nonparametric approaches, leads to the main problem of assessing the representativeness of the available data for one type of event: convergence analysis applied to different statistical indicators is a rigorous strategy to assess the long-term stationarity of the heterogeneity represented in the training data. Nevertheless, the mathematical convergence is often too hard to be met on real data sets where the variables are not independent and identically distributed. A more pragmatic approach for routine data simulation is to consider a training data period representing events with a recurrence time longer than the simulated period and run a cross validation exercise as the one proposed in section 4.2 to test the reliability of the simulated ensemble. In particular, the *average quantile interval mismatch* (section 4.2) allows assessing whether the simulated variability is preserved, also for a nonstationary data set.

The simulated fields show overrepresentation of small rain cells associated to low rainfall amount. This is due to the generation of a moderate small-scale noise intrinsic to the process of resampling. This phenomenon has minimal quantitative relevance since there is no significant added rainfall amount or bias in the other statistics. It could be removed with postprocessing, such as moving average filtering or object-based analysis, but this type of operations should be used with caution to avoid introducing more important artifacts in the simulated fields.

When conditioned by a known weather scenario, the technique can preserve the temporal weather-type patterns thanks to the use of the CTIS, chosen on the basis of weather indicators. Among these indicators, the computation of the variable *C*, categorizing the rainfall event, is very accurate since it is based on the reference images that indicate precisely not only the rainfall type (NW or SE) but also the intensity class (weak, moderate, or strong). The choice of the appropriate weather indicators relies on the knowledge of the rainfall types and climate dynamics characterizing the study region. The presented setup is specific for the study region, but can be adapted to other regions of interest after an accurate study of the daily nonstationarity of rainfall. Additional information about the daily weather conditions may be included as auxiliary variables to make a proper characterization of the weather types present in the region. The main advantages of this approach with respect to previous techniques based on weather conditioning (section 1) are the following:

1. The mathematical framework is significantly simplified with respect to previously mentioned simulation approaches (e.g., Hewitson & Crane, 2002; Hughes et al., 1999; Langousis et al., 2016; Langousis & Kaleris, 2014; Vrac et al., 2007) since it is not based on explicit parametric modeling, while it is focused on preserving the similarity of data patterns; as a consequence, the weather conditioning scheme can be much more complex, including continuous or categorical variables, also carrying soft or incomplete information, with no need of variable transformation and the only assumption of representativity of the training data set.
2. By applying a variable data-pattern conditioning and a random simulation path, the first data are simulated at sparse time locations accounting of far neighbor patterns, then progressively filling up the time series using closer time steps as conditioning data. This allows preserving multiple-scale statistics and nonlinear behavior in the temporal succession of weather types, instead of being limited to the fixed and generally low-order time dependence of a Markov-chain framework. As a result, Figure 6 together with the indicator $B_{0.05,0.95}$ shows the efficiency in targeting the precise weather conditions for every day and estimating the temporal variability over a nonstationary weather time series.
3. The choice of CTIS is not constant for all days presenting the same weather type, but dynamic and based on the daily weather pattern of the current and neighbor days, accommodating nonstationary climate transitions. Using the presented setup, the conditional training images chosen for a day will present a similar pattern of weather classes for the neighbor days and similar temperature-data patterns. The probability to select certain training images with the gradual change of the data patterns allows smooth climatic transitions, similarly to what was proposed in Langousis et al. (2016) with a more complex parametric approach.

Nevertheless, the technique carries some specific limitations:

1. To generate a sufficient variety of daily weather patterns, the technique should dispose of a representative catalog of training images. It is possible to simulate long-term climate conditions different from the one observed in the climatic record (see e.g., Oriani et al., 2017, Figure 8) by rearranging the temporal weather patterns, but it is not possible to simulate daily weather conditions not present in the historical record. This limitation may be soften with a parametric approach capable of extrapolating weather characteristics to a nonobserved extent.
2. Since the conditioning temporal pattern for the choice of the CTIS varies from one simulated time step to another, the time dependency is less controlled than parametric techniques. As shown for rainfall time series in Oriani et al. (2017), a fixed time-dependency approach may be more efficient in case of scarce training data and if a simple temporal structure exists.
3. The method, based on an iterative scan of the training data, tend to be significantly slower than parametric approaches, especially in the generation of spatial fields. For instance, generating with a personal computer a raster image of 15,000–20,000 pixels, as done in the presented experiments, can take from a few seconds to several minutes; the computation time depends on the complexity of the auxiliary variables employed, the size of the scanned training data set, and the search neighborhood parameters. The used implementation (Straubhaar, 2011) is compatible with parallel-computation architectures to speed up the simulation process.
4. Rainfall fields at the daily 1-km resolution can be used in engineering and hydrological problems involving long-term processes with a rather high spatial detail: for example, to quantify the seasonal spatial patterns of infiltration, mean evapotranspiration, soil moisture, and erosion over complex terrains. For other applications, such as studying the short-term response of small fast-responding watersheds, it is necessary to model the rainfall process at higher temporal resolution. In this case, preserving the rainfall-cell advection becomes a relevant issue that requires the generated fields to be explicitly correlated in time. The proposed technique needs substantial modifications to be adapted for this purpose, i.e., by extending the data-pattern resampling scheme in both space and time.

If the radar image record is totally or partially missing, the technique can still be applied using other source of information to define the weather categories, e.g., satellite precipitation estimates, ground measurements, or climate model output data, but it may lead to a less precise CTIS selection. If the conditioning climatic time series for the simulation period is partially or totally missing, the same technique can be used to generate it together with the CTIS (step 1 of the technique, section 3.2). In the absence of any conditioning data, the simulated weather time series would be stationary and preserve the statistics of the training data (see the previous tests on rainfall time series simulation; Oriani et al., 2014). As other simulation algorithms, this approach can be applied in a conditional simulation setting, if the rainfall amount is known at certain locations: DS considers the data given at certain locations as already simulated and completes the field with no modification in the workflow. This type of simulation can be used to regenerate portions of radar image presenting artifacts or missing data. A similar application to satellite imagery can be found in Mariethoz and Renard (2010).

6. Conclusions

In this paper, a novel technique is proposed to generate stochastic rain fields reproducing the observed daily spatial variability of rainfall for a known weather scenario. The core of the methodology is the use of the direct sampling technique (DS) together with rainfall radar fields used as training images and a series of climate indicators used as conditioning variables. DS, a resampling technique belonging to multiple-point geostatistics, simulates the variable of interest by scanning a training image (TI). Considering patterns of different size throughout the course of the simulation, DS is capable of generating realistic structures at multiple scales.

Since the daily spatial rainfall is highly nonstationary, the simple application of DS with the entire set of historical TIs is not appropriate to simulate the weather for a specific day. For this reason, the proposed methodology is composed of two steps: (1) using DS, a subset of training images are sampled, which present the same type of weather pattern for a given day, according to a series of climate indicators. In this way, a conditional training image set (CTIS) is retrieved for each day. Then, (2) DS is used again to generate an ensemble of spatial rainfall fields using the CTIS as training image. The algorithm setup proposed for this

operation includes the topographic elevation as conditioning variable to preserve the related spatial variability of rainfall.

The methodology, tested on the simulation of the rainfall heterogeneity over a 15,000 km^2 semiarid region in the eastern Mediterranean, generates rain fields presenting a realistic spatial structure and correlation length. With minimal complexity in the parameterization, the statistical relation with elevation is preserved, delineating a different rainfall amount distribution for the coastal, mountainous, and Jordan Valley zones.

The technique can be adapted to different climate settings by including in the setup the appropriate set of weather indicators, describing different weather types or a continuous variability. This requires an accurate investigation of the local weather, possibly connected to the synoptic climate conditions. In the presence of a highly nonstationary heterogeneity, the introduction of CTIS turns out to be an effective addition to multiple-point simulation since it allows extracting a subset of the training data representing the local variability, which otherwise would be dispersed in a too vast data set. This feature can be incorporated in other environmental applications where temporal or spatial trends and periodicity are represented with the help of predictive indicators.

Acknowledgments
This research was initiated in the framework of the Swiss National Science Foundation (SNF) project 200021_134614, pursued within the SNF project P2NEP2_162040, the European Union's Horizon 2020 research and innovation program project 641762 (ECOPOTENTIAL), and the Lady Davis Fellowship Trust (project: RainFreq). The radar imagery is provided by the E.M.S. Company (http://www.emsmekorotprojects.com/), temperature and elevation data by the Israel Meteorological Service (IMS) (http://www.ims.gov.il), and elevation data are provided by the Survey of Israel (http://mapi.gov.il).

References

Aghakouchak, A., Habib, E., & Bardossy, A. (2010). Modeling radar rainfall estimation uncertainties: Random error model. *Journal of Hydrologic Engineering*, *15*(4), 265–274. https://doi.org/10.1061/(ASCE)HE.1943-5584.0000185

Argueso, D., Manuel Hidalgo-Munoz, J., Raquel Gamiz-Fortis, S., Jesus Esteban-Parra, M., & Castro-Diez, Y. (2012). Evaluation of WRF mean and extreme precipitation over Spain: Present climate (1970-99). *Journal of Climate*, *25*(14), 4883–4897. https://doi.org/10.1175/JCLI-D-11-00276.1

Arnaud, P., Bouvier, C., Cisneros, L., & Dominguez, R. (2002). Influence of rainfall spatial variability on flood prediction. *Journal of Hydrology*, *260*(1–4), 216–230. https://doi.org/10.1016/S0022-1694(01)00611-4

Bardossy, A., & Pegram, G. (2013). Interpolation of precipitation under topographic influence at different time scales. *Water Resources Research*, *49*, 4545–4565. https://doi.org/10.1002/wrcr.20307

Beckmann, B.-R., & Adri Buishand, T. (2002). Statistical downscaling relationships for precipitation in the Netherlands and north Germany. *International Journal of Climatology*, *22*(1), 15–32.

Benoit, L., & Mariethoz, G. (2017). Generating synthetic rainfall with geostatistical simulations, *Wiley Interdisciplinary Reviews: Water*, *4*, e1199.

Berg, P., Moseley, C., & Haerter, J. O. (2013). Strong increase in convective precipitation in response to higher temperatures. *Nature Geoscience*, *6*(3), 181–185.

Bonnifait, L., Delrieu, G., Le Lay, M., Boudevillain, B., Masson, A., Belleudy, P., . . . Saulnier, G.-M. (2009). Distributed hydrologic and hydraulic modelling with radar rainfall input: Reconstruction of the 8–9 September 2002 catastrophic flood event in the Gard Region, France. *Advances in Water Resources*, *32*(7), 1077–1089.

Borga, M., Anagnostou, E., Blöschl, G., & Creutin, J.-D. (2011). Flash flood forecasting, warning and risk management: The hydrate project. *Environmental Science & Policy*, *14*(7), 834–844.

Buishand, T. A., & Brandsma, T. (2001). Multisite simulation of daily precipitation and temperature in the Rhine Basin by nearest-neighbor resampling. *Water Resources Research*, *37*(11), 2761–2776. https://doi.org/10.1029/2001WR000291

Bullock, J., Russell, O., Alapaty, K., Herwehe, J. A., Mallard, M. S., Otte, T. L., . . . Nolte, C. G. (2014). An observation-based investigation of nudging in WRF for downscaling surface climate information to 12-km grid spacing. *Journal of Applied Meteorology and Climatology*, *53*(1), 20–33. https://doi.org/10.1175/JAMC-D-13-030.1

C2SM, MeteoSwiss, ETH, NCCR Climate, and OcCC. (2011). *Swiss climate change scenarios CH2011*. Zurich, Switzerland: C2SM.

Caldwell, P., Chin, H.-N. S., Bader, D. C., & Bala, G. (2009). Evaluation of a WRF dynamical downscaling simulation over California. *Climatic Change*, *95*(3–4), 499–521. https://doi.org/10.1007/s10584-009-9583-5

Carpenter, T. M., & Georgakakos, K. P. (2004). Impacts of parametric and radar rainfall uncertainty on the ensemble streamflow simulations of a distributed hydrologic model. *Journal of Hydrology*, *298*(1), 202–221.

Corte-Real, J., Xu, H., & Qian, B. (1999). A weather generator for obtaining daily precipitation scenarios based on circulation patterns. *Climate Research*, *13*(1), 61–75.

Creutin, J., Delrieu, G., & Lebel, T. (1988). Rain measurement by raingage—Radar combination: A geostatistical approach. *Journal of Atmospheric and Oceanic Technology*, *5*(1), 102–115.

Drobinski, P., Silva, N. D., Panthou, G., Bastin, S., Muller, C., Ahrens, B., . . . Torma, C. Z. (2016). Scaling precipitation extremes with temperature in the Mediterranean: Past climate assessment and projection in anthropogenic scenarios. *Climate Dynamics*, 1–21. https://doi.org/10.1007/s00382-016-3083-x

Duckstein, L., Fogel, M. M., & Kisiel, C. C. (1972). A stochastic model of runoff-producing rainfall for summer type storms. *Water Resources Research*, *8*(2), 410–421.

Faures, J., Goodrich, D., Woolhiser, D., & Sorooshian, S. (1995). Impact of small-scale spatial rainfall variability on runoff modeling. *Journal of Hydrology*, *173*(1–4), 309–326. https://doi.org/10.1016/0022-1694(95)02704-S

Fealy, R., & Sweeney, J. (2007). Statistical downscaling of precipitation for a selection of sites in Ireland employing a generalised linear modelling approach. *International Journal of Climatology*, *27*(15), 2083–2094.

Fowler, H., Blenkinsop, S., & Tebaldi, C. (2007). Linking climate change modelling to impacts studies: Recent advances in downscaling techniques for hydrological modelling. *International Journal of Climatology*, *27*(12), 1547–1578.

Fowler, H., Kilsby, C., O'connell, P., & Burton, A. (2005). A weather-type conditioned multi-site stochastic rainfall model for the generation of scenarios of climatic variability and change. *Journal of Hydrology*, *308*(1), 50–66.

Furrer, E. M., & Katz, R. W. (2007). Generalized linear modeling approach to stochastic weather generators. *Climate Research*, *34*(2), 129–144.

Germann, U., Berenguer, M., Sempere-Torres, D., & Zappa, M. (2009). Real-ensemble radar precipitation estimation for hydrology in a mountainous region. *Quarterly Journal of the Royal Meteorological Society*, *135*(639), 445–456. https://doi.org/10.1002/qj.375

Gupta, V. K., & Waymire, E. C. (1979). Stochastic kinematic study of subsynoptic space-time rainfall. *Water Resources Research*, *15*(3), 637–644. https://doi.org/10.1029/WR015i003p00637

Hasan, M. M., Sharma, A., Mariethoz, G., Johnson, F., & Seed, A. (2016). Improving radar rainfall estimation by merging point rainfall measurements within a model combination framework. *Advances in Water Resources*, *97*, 205–218.

He, X., Vejen, F., Stisen, S., Sonnenborg, T. O., & Jensen, K. H. (2011). An operational weather radar-based quantitative precipitation estimation and its application in catchment water resources modeling. *Vadose Zone Journal*, *10*(1), 8–24. https://doi.org/10.2136/vzj2010.0034

Hewitson, B., & Crane, R. (2002). Self-organizing maps: Applications to synoptic climatology. *Climate Research*, *22*(1), 13–26.

Hong, K.-O., Suh, M.-S., & Rha, D.-K. (2006). Temporal and spatial variations of precipitation in South Korea for recent 30 years (1976–2005) geographic environments. *The Journal of the Korean Earth Science Society*, *27*(4), 433–449.

Hughes, J., Guttorp, P., & Charles, S. (1999). A non-homogeneous hidden Markov model for precipitation occurrence. *Journal of the Royal Statistical Society: Series C, Applied Statistics*, *48*(1), 15–30.

Hyndman, R. J., & Grunwald, G. K. (2000). Applications: Generalized additive modelling of mixed distribution Markov models with application to Melbourne's rainfall. *Australian & New Zealand Journal of Statistics*, *42*(2), 145–158.

Jha, S. K., Mariethoz, G., Evans, J., McCabe, M. F., & Sharma, A. (2015). A space and time scale-dependent nonlinear geostatistical approach for downscaling daily precipitation and temperature. *Water Resources Research*, *51*, 6244–6261. https://doi.org/10.1002/2014WR016729

Jones, P., Kilsby, C., Harpham, C., Glenis, V., & Burton, A. (2009). *UK climate projections science report: Projections of future daily climate for the UK from the weather generator* (technical report). Callaghan, NSW, Australia: University of Newcastle.

Kafle, H. K., & Bruins, H. J. (2009). Climatic trends in Israel 1970–2002: Warmer and increasing aridity inland. *Climatic Change*, *96*(1), 63–77. https://doi.org/10.1007/s10584-009-9578-2

Kahana, R., Ziv, B., Enzel, Y., & Dayan, U. (2002). Synoptic climatology of major floods in the Negev Desert, Israel. *International Journal of Climatology*, *22*(7), 867–882. https://doi.org/10.1002/joc.766

Karnieli, A. (1990). Application of kriging technique to areal precipitation mapping in Arizona. *GeoJournal*, *22*(4), 391–398. https://doi.org/10.1007/BF00174760

Kilsby, C. G., Jones, P. D., Burton, A., Ford, A. C., Fowler, H. J., Harpham, C., . . . Wilby, R. L. (2007). A daily weather generator for use in climate change studies. *Environmental Modelling & Software*, *22*(12), 1705–1719. https://doi.org/10.1016/j.envsoft.2007.02.005

Kim, J.-W., & Pachepsky, Y. A. (2010). Reconstructing missing daily precipitation data using regression trees and artificial neural networks for swat streamflow simulation. *Journal of Hydrology*, *394*(3), 305–314.

Kim, S., Tachikawa, Y., Sayama, T., & Takara, K. (2009). Ensemble flood forecasting with stochastic radar image extrapolation and a distributed hydrologic model. *Hydrological Processes*, *23*(4), 597–611. https://doi.org/10.1002/hyp.7188

Krajewski, W. F. (1987). Cokriging radar-rainfall and rain-gauge data. *Journal of Geophysical Research*, *92*(D8), 9571–9580. https://doi.org/10.1029/JD092iD08p09571

Langousis, A., & Kaleris, V. (2014). Statistical framework to simulate daily rainfall series conditional on upper-air predictor variables. *Water Resources Research*, *50*, 3907–3932. https://doi.org/10.1002/2013WR014936

Langousis, A., Mamalakis, A., Deidda, R., & Marrocu, M. (2016). Assessing the relative effectiveness of statistical downscaling and distribution mapping in reproducing rainfall statistics based on climate model results. *Water Resources Research*, *52*, 471–494. https://doi.org/10.1002/2015WR017556

Leblois, E., & Creutin, J.-D. (2013). Space-time simulation of intermittent rainfall with prescribed advection field: Adaptation of the turning band method. *Water Resources Research*, *49*, 3375–3387. https://doi.org/10.1002/wrcr.20190

Maraun, D., F., Wetterhall, A., Ireson, R., Chandler, E., Kendon, M., Widmann, S., . . . Thiele-Eich, I. (2010). Precipitation downscaling under climate change: Recent developments to bridge the gap between dynamical models and the end user. *Reviews of Geophysics*, *48*, RG3003. https://doi.org/10.1029/2009RG000314

Mariethoz, G., & Renard, P. (2010). Reconstruction of incomplete data sets or images using direct sampling. *Mathematical Geosciences*, *42*(3), 245–268. https://doi.org/10.1007/s11004-010-9270-0

Mariethoz, G., Renard, P., & Straubhaar, J. (2010). The direct sampling method to perform multiple-point geostatistical simulations. *Water Resources Research*, *46*, W11536, https://doi.org/10.1029/2008WR007621

Marra, F., & Morin, E. (2015). Use of radar QPE for the derivation of intensity–duration–frequency curves in a range of climatic regimes. *Journal of Hydrology*, *531*, 427–440.

Marra, F., Morin, E., Peleg, N., Mei, Y., & Anagnostou, E. N. (2016a). Comparing intensity–duration–frequency curves derived from CMORPH and radar rainfall estimates over the eastern Mediterranean. *Hydrology and Earth System Sciences Discussions*, *2016*, 1–26. https://doi.org/10.5194/hess-2016-597

Marra, F., Nikolopoulos, E., Creutin, J., & Borga, M. (2016b). Space–time organization of debris flows-triggering rainfall and its effect on the identification of the rainfall threshold relationship. *Journal of Hydrology*, *541*, Part A, 246–255. https://doi.org/10.1016/j.jhydrol.2015.10.010

Marra, F., Nikolopoulos, E. I., Creutin, J. D., & Borga, M. (2014). Radar rainfall estimation for the identification of debris-flow occurrence thresholds. *Journal of Hydrology*, *519*, 1607–1619.

Meerschman, E., Pirot, G., Mariethoz, G., Straubhaar, J., Van Meirvenne, M., & Renard, P. (2013). A practical guide to performing multiple-point statistical simulations with the direct sampling algorithm. *Computers & Geosciences*, *52*, 307–324. https://doi.org/10.1016/j.cageo.2012.09.019

Northrop, P. (1996). *Modelling and statistical analysis of spatial-temporal rainfall fields* (PhD thesis). London, UK: Department of Statistical Science, University College London.

Onof, C., Chandler, R., Kakou, A., Northrop, P., Wheater, H., & Isham, V. (2000). Rainfall modelling using Poisson-cluster processes: A review of developments. *Stochastic Environmental Research and Risk Assessment*, *14*(6), 384–411.

Oriani, F. (2015). *Stochastic simulation of rainfall and climate variables using the direct sampling technique* (PhD thesis). Neuchâtel, Switzerland: Université de Neuchâtel.

Oriani, F., Mehrotra, R., Mariethoz, G., Straubhaar, J., Sharma, A., & Renard, P. (2017). Simulating rainfall time-series: How to account for statistical variability at multiple scales? *Stochastic Environmental Research and Risk Assessment*, 1–20. https://doi.org/10.1007/s00477-017-1414-z

Oriani, F., Straubhaar, J., Renard, P., & Mariethoz, G. (2014). Simulation of rainfall time series from different climatic regions using the direct sampling technique. *Hydrology and Earth System Sciences*, *18*(8), 3015–3031. https://doi.org/10.5194/hess-18-3015-2014

Orlowsky, B., Gerstengarbe, F.-W., & Werner, P. (2008). A resampling scheme for regional climate simulations and its performance compared to a dynamical RCM. *Theoretical and Applied Climatology*, *92*(3), 209–223.

Paschalis, A., Molnar, P., Fatichi, S., & Burlando, P. (2013). A stochastic model for high-resolution space-time precipitation simulation. *Water Resources Research*, *49*, 8400–8417. https://doi.org/10.1002/2013WR014437

Peleg, N., Marra, F., Fatichi, S., Paschalis, A., Molnar, P., & Burlando, P. (2017). Spatial variability of extreme rainfall at radar subpixel scale. *Journal of Hydrology*. https://doi.org/10.1016/j.jhydrol.2016.05.033, in press.

Peleg, N., & Morin, E. (2012). Convective rain cells: Radar-derived spatiotemporal characteristics and synoptic patterns over the eastern Mediterranean. *Journal of Geophysical Research*, *117*, D15116. https://doi.org/10.1029/2011JD017353

Peleg, N., & Morin, E. (2014). Stochastic convective rain-field simulation using a high-resolution synoptically conditioned weather generator (HiReS-WG). *Water Resources Research*, *50*, 2124–2139. https://doi.org/10.1002/2013WR014836

Putthividhya, A., & Tanaka, K. (2013). Optimal rain gauge network design and spatial precipitation mapping based on geostatistical analysis from co-located elevation and humidity data. *Chiang Mai Journal of Science*, *40*(2), 187–197.

Renard, P., Straubhaar, J., Caers, J., & Mariethoz, G. (2011). Conditioning facies simulations with connectivity data. *Mathematical Geosciences*, *43*(8), 879–903. https://doi.org/10.1007/s11004-011-9363-4

Rientjes, T., Haile, A. T., & Fenta, A. A. (2013). Diurnal rainfall variability over the Upper Blue Nile Basin: A remote sensing based approach. *International Journal of Applied Earth Observation and Geoinformation*, *21*, 311–325. https://doi.org/10.1016/j.jag.2012.07.009

Russo, F., Lombardo, F., Napolitano, F., & Gorgucci, E. (2006). Rainfall stochastic modeling for runoff forecasting. *Physics and Chemistry of the Earth*, *31*(18), 1252–1261. https://doi.org/10.1016/j.pce.2006.06.002

Sanchez-Moreno, J. F., Mannaerts, C. M., & Jetten, V. (2014). Influence of topography on rainfall variability in Santiago Island, Cape Verde. *International Journal of Climatology*, *34*(4), 1081–1097. https://doi.org/10.1002/joc.3747

Sarangi, A., Cox, C. A., & Madramootoo, C. A. (2005). Geostatistical methods for prediction of spatial variability of rainfall in a mountainous region. *Transactions of the ASAE*, *48*(3), 943–954.

Schleiss, M., Chamoun, S., & Berne, A. (2014). Nonstationarity in intermittent rainfall: The ''dry drift.'' *Journal of Hydrometeorology*, *15*(3), 1189–1204. https://doi.org/10.1175/JHM-D-13-095.1

Segond, M.-L., Wheater, H. S., & Onof, C. (2007). The significance of spatial rainfall representation for flood runoff estimation: A numerical evaluation based on the lee catchment, UK. *Journal of Hydrology*, *347*(1–2), 116–131. https://doi.org/10.1016/j.jhydrol.2007.09.040

Shah, S., O'connell, P., & Hosking, J. (1996). Modelling the effects of spatial variability in rainfall on catchment response. 1. Formulation and calibration of a stochastic rainfall field model. *Journal of Hydrology*, *175*(1), 67– 88. https://doi.org/10.1016/S0022-1694(96)80006-0

Sideris, I. V., Gabella, M., Erdin, R., & Germann, U. (2014). Real-time radar-rain-gauge merging using spatio-temporal co-kriging with external drift in the Alpine terrain of Switzerland. *Quarterly Journal of the Royal Meteorological Society*, *140*(680), 1097–1111. https://doi.org/10.1002/qj.2188

Sinclair, S., & Pegram, G. (2005). Combining radar and rain gauge rainfall estimates using conditional merging. *Atmospheric Science Letters*, *6*(1), 19–22. https://doi.org/10.1002/asl.85

Straubhaar, J. (2011). *MPDS technical reference guide*. Neuchâtel, Switzerland: Centre d'Hydrogeologie et de Geothermie, University of Neuchâtel.

Swain, M. J., & Ballard, D. H. (1991). Color indexing. *International Journal of Computer Vision*, *7*(1), 11–32.

Syed, K. H., Goodrich, D. C., Myers, D. E., & Sorooshian, S. (2003). Spatial characteristics of thunderstorm rainfall fields and their relation to runoff. *Journal of Hydrology*, *271*(1–4), 1–21. https://doi.org/10.1016/S0022-1694(02)00311-6

Todini, E. (1999). A Bayesian technique for conditioning radar precipitation estimates to rain-gauge measurements. *Hydrology and Earth System Sciences*, *5*(2), 187–199.

Tsvieli, Y., & Zangvil, A. (2005). Synoptic climatological analysis of wet and dry Red Sea troughs over Israel. *International Journal of Climatology*, *25*(15), 1997–2015. https://doi.org/10.1002/joc.1232

Velasco-Forero, C. A., Sempere-Torres, D., Cassiraga, E. F., & Jaime Gomez-Hernandez, J. (2009). A non-parametric automatic blending methodology to estimate rainfall fields from rain gauge and radar data. *Advances in Water Resources*, *32*(7), 986–1002. https://doi.org/10.1016/j.advwatres.2008.10.004

Vrac, M., Stein, M., & Hayhoe, K. (2007). Statistical downscaling of precipitation through nonhomogeneous stochastic weather typing. *Climate Research*, *34*(3), 169–184.

Wesson, S. M., & Pegram, G. G. (2004). Radar rainfall image repair techniques. *Hydrology and Earth System Sciences Discussions*, *8*(2), 220–234.

Wilby, R. L., Conway, D., & Jones, P. (2002). Prospects for downscaling seasonal precipitation variability using conditioned weather generator parameters. *Hydrological Processes*, *16*(6), 1215–1234.

Wilson, C. B., Valdes, J. B., & Rodriguez-Iturbe, I. (1979). Influence of the spatial-distribution of rainfall on storm runoff. *Water Resources Research*, *15*(2), 321–328. https://doi.org/10.1029/WR015i002p00321

Wojcik, R., McLaughlin, D., Konings, A., & Entekhabi, D. (2009). Conditioning stochastic rainfall replicates on remote sensing data. *IEEE Transactions on Geoscience and Remote Sensing*, *47*(8), 2436–2449.

Woolhiser, D. A., & Goodrich, D. C. (1988). Effect of storm rainfall intensity patterns on surface runoff. *Journal of Hydrology*, *102*(1–4), 335–354. https://doi.org/10.1016/0022-1694(88)90106-0

Yakir, H., & Morin, E. (2011). Hydrologic response of a semi-arid watershed to spatial and temporal characteristics of convective rain cells. *Hydrology and Earth System Sciences*, *15*(1), 393–404.

Yang, C., Chandler, R., Isham, V., & Wheater, H. (2005). Spatial-temporal rainfall simulation using generalized linear models. *Water Resources Research*, *41*, W11415. https://doi.org/10.1029/2004WR003739

Yoon, S.-S., & Bae, D.-H. (2013). Optimal rainfall estimation by considering elevation in the Han River Basin, South Korea. *Journal of Applied Meteorology and Climatology*, *52*(4), 802–818. https://doi.org/10.1175/JAMC-D-11-0147.1

Zhang, C., Wang, Y., Lauer, A., & Hamilton, K. (2012). Configuration and evaluation of the WRF model for the study of Hawaiian regional climate. *Monthly Weather Review*, *140*(10), 3259–3277. https://doi.org/10.1175/MWR-D-11-00260.1

Zhang, Y., & Held, I. M. (1999). A linear stochastic model of a GCMS midlatitude storm tracks. *Journal of the Atmospheric Sciences*, *56*(19), 3416–3435.

Zhang, Z., & Switzer, P. (2007). Stochastic space-time regional rainfall modeling adapted to historical rain gauge data. *Water Resources Research*, *43*, W03441. https://doi.org/10.1029/2005WR004654